Kuratite, $Ca_4(Fe^{2+}_{10}Ti_2)O_4[Si_8Al_4O_{36}]$, the Fe^{2+}-analogue of rhönite, a new mineral from the D'Orbigny angrite meteorite

S.-L. Hwang[1,*], P. Shen[2], H.-T. Chu[3], T.-F. Yui[4], M.-E. Varela[5] and Y. Iizuka[4]

[1] Department of Materials Science and Engineering, National Dong Hwa University, Hualien, Taiwan, ROC
[2] Department of Materials Science and Optoelectronic Science, National Sun Yat-sen University, Kaohsiung, Taiwan, ROC
[3] Central Geological Survey, PO Box 968, Taipei, Taiwan, ROC
[4] Institute of Earth Sciences, Academia Sinica, Taipei, Taiwan, ROC
[5] Instituto de Ciencias Astronómicas de la Tierra y del Espacio (ICATE) Avenida España 1512 sur, J5402DSP, San Juan, Argentina

ABSTRACT

Kuratite, ideally $Ca_4(Fe^{2+}_{10}Ti_2)O_4[Si_8Al_4O_{36}]$, the Fe^{2+}-analogue of rhönite and a new member of the sapphirine supergroup, was identified from the D'Orbigny angrite meteorite by electron microscopy and micro-Raman spectroscopy. Based on the least-squares refinement of 25 d-spacings measured from selected-area electron diffraction patterns of 11 zone axes, the symmetry of kuratite was shown to be triclinic (space group $P\bar{1}$ by analogy to rhönite) with $a = 10.513(7)$, $b = 10.887(7)$, $c = 9.004(18)$ Å, $\alpha = 105.97(13)$, $\beta = 96.00(12)$, $\gamma = 124.82(04)°$, $V = 767 \pm 2$ Å^3 and $Z = 1$ for the 40 oxygen formula. The empirical formula based on eight electron microprobe analyses is $(Ca_{3.88}Na_{0.02}REE^{3+}_{0.03}Mn_{0.03}Mg_{0.01}Ni_{0.02}Zn_{0.01}Sr_{0.01})_{\Sigma4.01}$ $(Fe^{2+}_{9.98}9.9Ti_{2.00})_{\Sigma11.98}(Si_{7.80}Al_{3.52}Fe^{3+}_{0.64}P_{0.05}S_{0.02})_{\Sigma12.03}O_{39.98}F_{0.01}Cl_{0.01}$. The simplified formula is $Ca_4(Fe^{2+}_{10}Ti_2)O_4[Si_8Al_4O_{36}]$. Micro-Raman spectroscopy showed four main bands resembling those of lunar rhönite but with higher frequencies due to different chemical composition. Analogous to the occurrence of kuratite in terrestrial basaltic rocks, kuratite coexisting with Al, Ti-bearing hedenbergite, ulvöspinel, iron-sulfide, tsangpoite, Ca-rich fayalite and kirschsteinite in D'Orbigny angrite most probably was formed at >1000°C by rapid cooling of an interstitial melt, which is subsilicic, almost Mg-free but enriched in Al-P-Ca-Ti-Fe.

Introduction

The sapphirine supergroup comprises the sapphirine and surinamite groups, which constitute a polysomatic series (Grew *et al.*, 2008). The sapphirine group is further divided into three subgroups according to the occupancy of the two largest *M* sites at boundaries of octahedral walls in the structure (Bonaccorsi *et al.*, 1990), namely, sapphirine (Mg), aenigmatite (Na) and rhönite (Ca). The rhönite subgroup comprises rhönite

$Ca_4(Mg_8Fe^{3+}_2Ti_2)O_4[Si_6Al_6O_{36}]$, dorrite $Ca_4(Mg_3Fe^{3+}_9)O_4[Si_3Al_8Fe^{3+}O_{36}]$, serendibite $Ca_4(Mg_6Al_6)O_4[Si_6B_3Al_3O_{36}]$, høgtuvaite $Ca_4(Fe^{2+}_6Fe^{3+}_6)O_4[Si_8Be_2Al_2O_{36}]$, makarochkinite $Ca_4(Fe^{2+}_8Fe^{3+}_2Ti_2)O_4[Si_8Be_2Al_2O_{36}]$, welshite $Ca_4(Mg_9Sb^{5+}_3)O_4[Si_6Be_3AlFe^{3+}O_{36}]$, the unnamed Ti^{3+}-bearing Mg analogue of rhönite $Ca_4(Mg_7AlTi^{3+}_2Ti^{4+}_2)O_4[Si_5Al_7O_{36}]$ and the unnamed Fe^{2+} analogue of rhönite $Ca_4(Fe^{2+}_{10}Ti_2)O_4[Si_8Al_4O_{36}]$ (Grew *et al.*, 2008, and references therein). The Fe^{2+} analogue of rhönite currently listed as a valid unnamed mineral with IMA code UM1972-18-SiO:AlCaFeMgTi (Smith and Nickel, 2007, and updates) has now been formally named kuratite in honour of Professor

* E-mail: slhwang@mail.ndhu.edu.tw

Dr Gero Kurat (1938–2009), former Head of the Mineralogical-Petrographical Department and Curator of the Meteorite Collection at the Natural History Museum in Vienna, Austria. He was a pioneer in meteorite research and a gifted mineralogist and petrologist. He identified the unusual D'Orbigny meteorite as an angrite. The new mineral and its name were approved by the IMA-CNMNC (IMA 013-109). Type material is deposited in the collections of the Naturhistorisches Museum Wien, Vienna, Austria, inventory number Section D'Orbigny C-N1172-NH Wien. Here we report the description and characterization of the new mineral kuratite, ideally $Ca_4(Fe^{2+}_{10}Ti_2)$ $O_4[Si_8Al_4O_{36}]$, the Fe^{2+} analogue of rhönite. The origin and formation conditions of kuratite in the angrite meteorite are also addressed, based on the available information on terrestrial kuratite occurrences.

Occurrence and appearance

Kuratite occurs in D'Orbigny, a 16.5 kg angrite meteorite found in July 1979 in Argentina. The polished angrite slab sample *c.* 1.5 cm × 1.5 cm × 0.3 cm in size used for the present study was kindly loaned by the Naturhistorisches Museum Wien, Austria. Petrography of the D'Orbigny angrite has been described in detail by Mittlefehldt *et al.* (2002), Kurat *et al.* (2004) and Varela *et al.* (2003). In addition to the presence of some hollow shells and open vesicles of various sizes and shapes with occasional glass filling, D'Orbigny angrite consists of the following silicate phase assemblage: tabular crystals of nearly pure anorthite, euhedral to anhedral augite crystals with Mg-free and Al, Ti-bearing hedenbergite rims, euhedral to anhedral olivine crystals with Mg-rich cores (Mg ~64 mol.%) and complex Ca-rich fayalite + kirschsteinite overgrowths toward the rims (Fig. 1*a,b*). The whole microstructure can be characteristically described as olivine + augite aggregates with highly irregular outlines suggestive of brittle fracture (as circled in Fig. 1*a*) surrounded by anorthite crystals. Pockets consisting of several phases with an overall brighter contrast in scanning electron microscope (SEM) back-scattered electron (BSE) imaging due to Fe sulfides and ulvöspinel are common along grain boundaries within the olivine + augite aggregates (Fig. 1*a,b*). Detailed SEM observations indicate that the multiple phase pockets sit mainly at olivine-augite triple junctions, and consist of: (1) Fe-sulfide spherules

and euhedral ulvöspinel; (2) fibrous Na-bearing anorthite; (3) fibrous whitlockite, which was described as Ca-phosphate (Mittlefehldt *et al.*, 2002); (4) the new mineral tsangpoite, approved recently by IMA-CNMNC and to be published in a separate paper (IMA 2014-110, $Ca_5(PO_4)_2SiO_4$, hexagonal; Hwang *et al.*, 2015), and previously described as silico-phosphate (Mittlefehldt *et al.*, 2002; Kurat *et al.*, 2004); (5) the new mineral kuratite, previously described as Fe-Ca-Al-Ti silicate (Mittlefehldt *et al.*, 2002), or Fe-Al-Ti silicate (Kurat *et al.*, 2004), or 'rhönite' (Jambon and Boudouma, 2011); and (6) Al, Ti-bearing hedenbergite filling vesicles (Fig. 1). Kuratite crystals are typically euhedral to anhedral, < 20 μm in size, and occur, together with whitlockite and submicrometre-sized Fe sulfide, within a rim of olivine of Ca-rich fayalite composition (Ca ≈ 20 mol.%) + kirschsteinite (Ca ≈ 40 mol.%) intergrowths at the contact between Fe-sulfide spherules and the Al, Ti-bearing hedenbergite filling vesicles (Fig. 1*c–e*). Such intergrowths were not observed at the contacts without hedenbergite between Fe-sulfide spherules and the olivine overgrowth rim enriched with Fe/Ca (Fig. 1*f*). Whitlockite inclusions in kuratite are common (Fig. 1*d,e*).

Chemical data

Chemical analyses were carried out using a JEOL JXA8500-F FE-electron microprobe at Academia Sinica, Taiwan (wavelength-dispersive spectroscopy mode, 12 kV, 5 nA, 2 μm beam diameter). Natural and synthetic standard minerals and diffracting crystals (in parenthesis) used for calibration were diopside for $SiK\alpha$ (TAP), rutile for $TiK\alpha$ (PET), corundum for $AlK\alpha$ (TAP), chromium oxide for $CrK\alpha$ (PET), hematite for $FeK\alpha$ (LiF), tephroite for $MnK\alpha$ (PET), periclase for $MgK\alpha$ (TAP), Ni oxide for $NiK\alpha$ (LiF), wollastonite for $CaK\alpha$ (PET), albite for $NaK\alpha$ (TAP), adularia for $KK\alpha$ (PET), apatite for $PK\alpha$ (PET), fluorite for $FK\alpha$ (TAP), tugtupite for $ClK\alpha$ (PET), celestite for $SK\alpha$ (PET), Zn oxide for $ZnK\alpha$ (LiF), celestite for $SrL\alpha$ (PET), YAl garnet (YAG) for $YL\alpha$ (PET), LaP_5O_{14} for $LaL\alpha$ (LiF), PrP_5O_{14} for $PrL\beta$ (LiF), NdP_5O_{14} for $NdL\beta$ (LiF). Counting times for the peak of each element and backgrounds both above and below peak were 20 and 10 s, respectively. Eight analyses of kuratite and their average are given in Table 1*a*. The empirical formula (atoms per formula unit) of the average, based on 28 cations and 40 oxygens, is
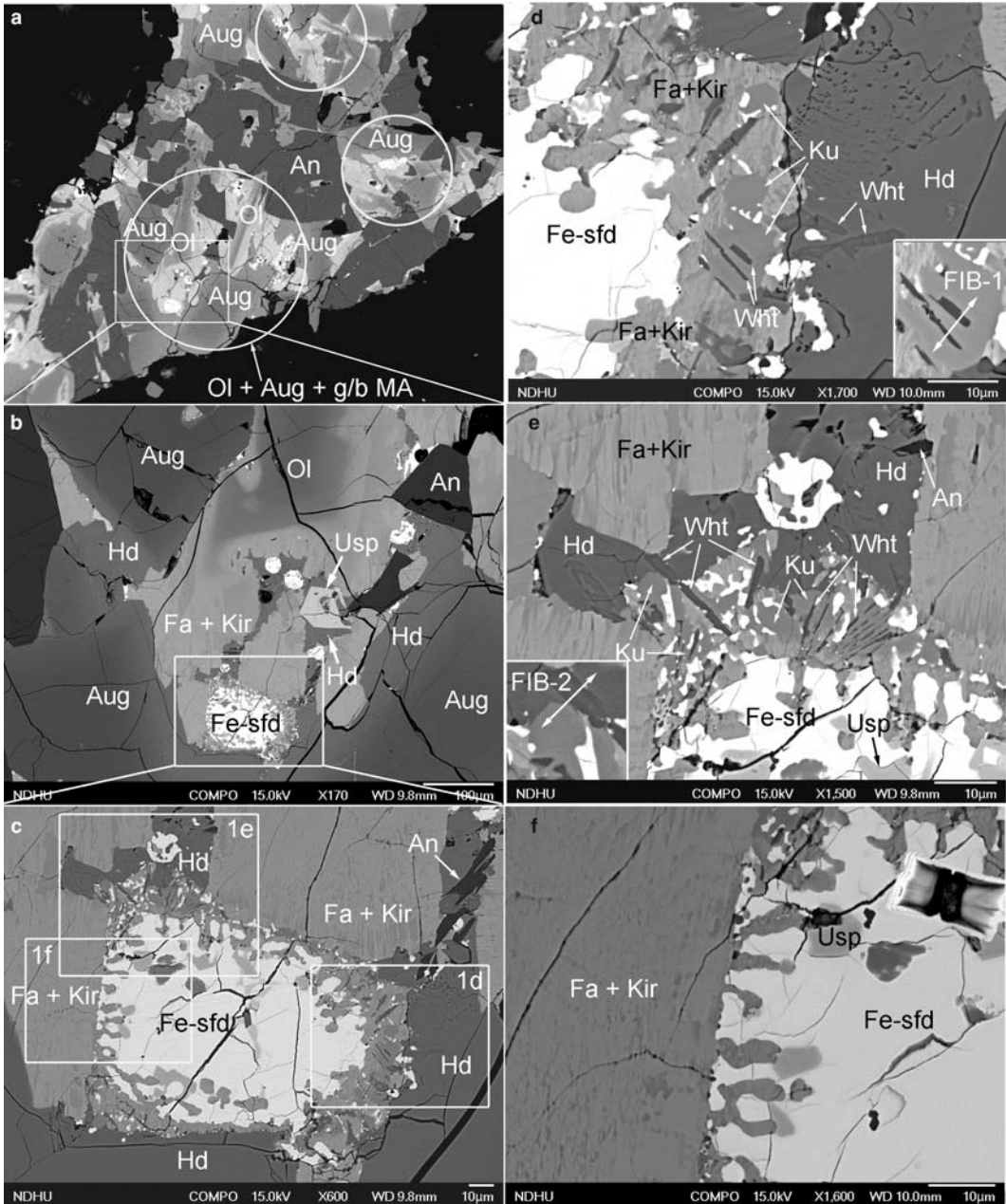
1068

FIG. 1. SEM-BSE micrographs showing (*a*) the ubiquitous presence of a multiple phase assemblage (MA) at the triple-junction of an olivine (Ol) + augite (Aug) grain aggregate (circled) with a highly irregular outline; (*b*) the main constituents of the multiple-phase assemblage, including Fe sulfide (Fe-sfd), ulvöspinel (Usp) and the Al, Ti-bearing hedenbergite (Hd), with complex Ca-rich fayalite (Fa) + kirschsteinite (Kir) overgrowths toward the olivine rims; (*c*), (*d*) and (*e*) kuratite (Ku) and whitlockite (Wht) crystals surrounded by Fe/Ca-olivine intergrowth at the periphery of Fe-sulfide spherule facing hedenbergite; (*c*) and (*f*) the absence of Ku + Wht at the Fe-sulfide boundary facing olivine. Note that fibrous whitlockite crystals are frequently enclosed by kuratite (*d*). Two FIB thin sections for electron diffraction study of kuratite structure are shown as inserts in (*d*) and (*e*).

1069

TABLE 1*a*. Chemical composition (wt.%) of kuratite from D'Orbigny angrite.

	B5-a-3	B5-a-4	B5-a-5	B5-a-6	B5-a-7	B5-a-8	B5-a-9	B5-a-10	Average
SiO_2	25.37	25.16	25.95	25.06	26.39	25.21	25.50	25.80	25.55
TiO_2	8.43	9.17	8.52	8.51	9.78	8.68	8.33	8.15	8.70
Al_2O_3	10.32	10.18	9.53	9.35	8.86	10.29	10.01	9.90	9.80
Cr_2O_3	0.00	0.00	0.00	0.00	0.00	0.00	0.11	0.00	0.01
Y_2O_3	0.08	0.00	0.05	0.04	0.03	0.00	0.00	0.00	0.03
La_2O_3	0.23	0.00	0.00	0.00	0.00	0.00	0.03	0.07	0.04
Pr_2O_3	0.15	0.00	0.22	0.00	0.18	0.12	0.06	0.00	0.09
Nd_2O_3	0.18	0.01	0.00	0.00	0.13	0.21	0.00	0.00	0.07
FeO Total	42.01	41.09	40.98	41.76	41.95	41.86	41.60	41.57	41.60
MnO	0.20	0.02	0.04	0.13	0.06	0.03	0.24	0.15	0.11
NiO	0.01	0.00	0.15	0.00	0.00	0.19	0.00	0.18	0.07
SrO	0.06	0.08	0.04	0.04	0.05	0.03	0.00	0.06	0.05
ZnO	0.00	0.00	0.00	0.00	0.22	0.00	0.03	0.10	0.04
MgO	0.00	0.02	0.00	0.06	0.00	0.02	0.00	0.01	0.01
CaO	11.92	11.86	11.84	11.78	11.56	12.10	11.96	11.82	11.86
Na_2O	0.00	0.02	0.13	0.03	0.01	0.00	0.07	0.04	0.04
K_2O	0.01	0.00	0.00	0.00	0.00	0.01	0.00	0.01	0.00
P_2O_5	0.27	0.16	0.20	0.23	0.08	0.17	0.19	0.27	0.20
F	0.00	0.00	0.00	0.00	0.00	0.02	0.03	0.00	0.01
Cl	0.03	0.00	0.02	0.04	0.03	0.04	0.00	0.01	0.02
SO_3	0.09	0.07	0.06	0.13	0.08	0.05	0.09	0.05	0.08
Total	99.36	97.82	97.72	97.16	99.42	99.01	98.23	98.19	98.38

$(Ca_{3.88}Na_{0.02}REE^{3+}_{0.03}Mn_{0.03}Mg_{0.01}Ni_{0.02}Zn_{0.01}$ $Sr_{0.01})_{\Sigma 4.01}(Fe^{2+}_{9.98}Ti_{2.00})_{\Sigma 11.98}(Si_{7.80}Al_{3.52}Fe^{3+}_{0.64}P_{0.05}$ $S_{0.02})_{\Sigma 12.03}O_{39.98}F_{0.01}Cl_{0.01}$ (Table 1*b*; *REE* = rare-earth minerals). Most analyses show the presence of 5–8% Fe^{3+} among all Fe analysed. The simplified formula is $Ca_4(Fe^{2+}_{10}Ti_2)O_4[Si_8Al_4O_{36}]$.

Crystallography

Two transmission electron microscopy (TEM) samples of dimensions 5 μm × 5 μm × 100 nm were prepared by the focused ion beam (FIB) technique from two kuratite grains (inserts in Fig. 1*d,e*). A JEOL 3010 analytical electron microscope (AEM) was used for imaging and energy-dispersive X-ray (EDX) analyses. Selected-area electron diffraction (SAED) patterns of kuratite were taken at various tilt angles for phase identification. A representative TEM bright field micrograph showing a kuratite crystal with abundant polysynthetic nano-twins and whitlockite inclusions in thin section FIB-1 is shown in Fig. 2*a*. Surrounding Fa + Kir intergrowths can also be clearly seen. The twin plane is $(0\bar{1}1)$, similar to that reported for other rhönite subgroup minerals.

In contrast, the kuratite crystal in thin section FIB-2 is twin-free and inclusion-free, and is associated with euhedral whitlockite and a rounded Fe sulfide within a polycrystalline hedenbergite matrix (Fig. 2*b*). Kuratite is bounded by small faces, such as $(0\bar{1}1)$, $(0\bar{2}1)$, $(0\bar{3}1)$ etc., as indicated in Fig. 2*c*.

Unit-cell parameters of kuratite were determined from SAED patterns. The error of the *d*-spacing measurements on electron diffraction patterns taken at a camera length of 120 cm and calibrated by an Al standard was estimated to be ± 0.002 nm. Based on the least-squares refinement of 25 *d*-spacings (Table 2) measured from eleven diffraction patterns of the twin-free kuratite crystal in section FIB-2 (insert in Fig. 1*e*; Fig. 2*c*), including the six shown in Fig. 3*a–f* and five not shown ($[0\bar{1}1]$, $[0\bar{1}2]$, $[0\bar{1}3]$, $[10\bar{2}]$, $[\bar{1}2\bar{2}]$), unit-cell parameters of kuratite were determined to be very similar to those of other rhönite subgroup minerals (see unit-cell data below; Table 3). In comparison to rhönite with abundant Mg^{2+} (Table 3), the slightly larger unit-cell parameters of kuratite must be due to Fe^{2+} replacing Mg^{2+} at the octahedral sites. Note that the double diffraction effect in electron diffraction usually prohibits quantitative determination of the

TABLE 1*b*. Calculated formula (atoms per formula unit) for the averaged composition of kuratite.

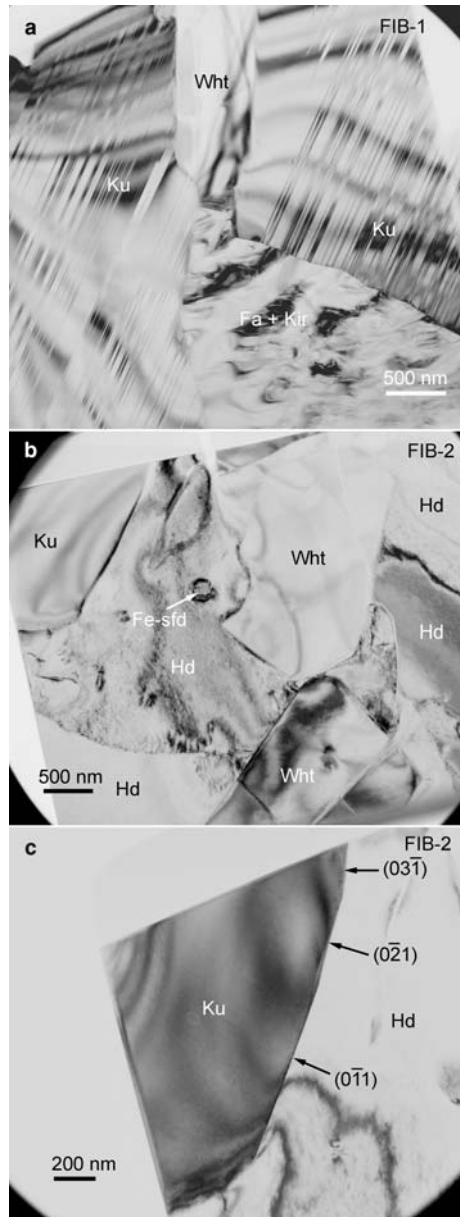| Constituent	wt.%	Symbol	No. ions	No. O atoms
SiO_2	25.55	Si^{4+}	7.796	15.593
TiO_2	8.70	Ti^{4+}	1.997	3.993
Al_2O_3	9.80	Al^{3+}	3.524	5.286
Cr_2O_3	0.01	Cr^{3+}	0.002	0.004
Y_2O_3	0.03	Y^{3+}	0.005	0.007
La_2O_3	0.04	La^{3+}	0.005	0.007
Pr_2O_3	0.09	Pr^{3+}	0.010	0.015
Nd_2O_3	0.07	Nd^{3+}	0.008	0.011
ΣFeO	41.60	ΣFe	10.615	10.933
FeO	39.10	Fe^{2+}	9.978	9.978
Fe_2O_3	2.77	Fe^{3+}	0.637	0.955
MnO	0.11	Mn^{2+}	0.028	0.028
NiO	0.07	Ni^{2+}	0.017	0.017
SrO	0.05	Sr^{2+}	0.009	0.009
ZnO	0.04	Zn^{2+}	0.009	0.009
MgO	0.01	Mg^{2+}	0.005	0.005
CaO	11.86	Ca^{2+}	3.877	3.908
Na_2O	0.04	Na^{+}	0.024	0.012
K_2O	0.00	K^{+}	0.000	0.000
P_2O_5	0.20	P^{5+}	0.052	0.129
F	0.01	F^{-}	0.010	
Cl	0.02	Cl^{-}	0.010	
SO_3	0.08	S^{6+}	0.018	0.055
O = Cl, F	–0.0087			
Total wt.%	98.37			
Σ				39.991
O = Cl, F				–0.010
Σ (O atoms)				39.981
Σ (cations)			27.999	
Σ (anions)				40.001

FIG. 2. TEM bright-field image showing (*a*) a kuratite crystal in thin section FIB-1 with abundant polysynthetic $(0\bar{1}1)$ nano-twins, which is associated with a whitlockite inclusion in a matrix of Fe/Ca-olivine intergrowths; (*b*) and (*c*) the twin-free kuratite crystal with $(0\bar{1}1)$, $(0\bar{2}1)$ and $(0\bar{3}1)$ facets in thin section FIB-2, with the associated euhedral whitlockite crystals, Fe sulfide, and the polycrystalline hedenbergite matrix.

relative intensities among the reflections. This is especially true for the low-order zone axis patterns such as $[00\bar{1}]$ and $[\bar{1}\,\bar{1}\,2]$, in which many reflections are present and double diffraction effects prevail (Fig. 3*a*,*b*). However, for the high-order zone-axis patterns with fewer reflections, the strong reflections can be nonetheless ascertained by careful examination, such as $22\bar{1}$ in the $[\bar{1}\,\bar{1}\,4]$ zone, $03\bar{1}$ and $\bar{2}5\bar{1}$ in the $[\bar{1}\,1\,3]$ zone, $\bar{2}4\bar{1}$ in the $[0\bar{1}\,4]$ zone, $\bar{1}1\bar{1}$ in the $[11\bar{3}]$ zone from section FIB-2 (Fig. 3*c*–*f*), as well as $4\bar{2}0$, $20\bar{3}$ and $21\bar{3}$ in the [362] and [364] zone axis patterns from section FIB-1 (Fig. 3*g*,*h*). It is no surprise that these strong reflections of kuratite are among the set of strong reflections in the X-ray diffraction data of makar-ochkinite, $Ca_4(Fe_8^{2+}Fe_2^{3+}Ti_2)O_4[Si_8Be_2Al_2O_{36}]$

1071

TABLE 2. Observed (obs) and refined (ref) *d*-spacings (Å) for kuratite from section FIB-2.

hkl	d_{obs}	d_{ref}	hkl	d_{obs}	d_{ref}
$1\bar{1}0$	9.43	9.436	$2\bar{3}1$	3.54	3.528
010	8.15	8.150	$1\bar{3}1$	3.50	3.496
100	8.14	8.143	111	3.41	3.404
$01\bar{1}$	7.51	7.512	$21\bar{1}$	3.22	3.229
$1\bar{1}1$	6.47	6.473	$21\bar{2}$	3.04	3.034
$2\bar{1}0$	5.17	5.159	$03\bar{1}$	2.97*	2.968
$1\bar{2}1$	5.14	5.144	$2\bar{4}1$	2.72*	2.716
$11\bar{1}$	4.90	4.895	$4\bar{2}0$	2.58*	2.580
110	4.51	4.516	211	2.50	2.497
$02\bar{1}$	4.45	4.448	$22\bar{1}$	2.44*	2.450
$2\bar{2}1$	4.25	4.256	$\bar{2}51$	2.13*	2.128
$\bar{2}01$	4.25	4.250	$\bar{4}1\bar{1}$	2.12*	2.116
$2\bar{1}1$	4.08	4.076			

*Strong reflections. Note that three strong reflections, 2.71 ($20\bar{3}$), 2.58 ($4\bar{2}0$) and 2.57 ($21\bar{3}$), were ascertained from diffraction patterns of section FIB-1. Reflections 2.71 ($20\bar{3}$) and 2.57 ($21\bar{3}$) were not recorded in diffraction patterns of section FIB-2 and hence not listed for unit-cell refinement.

(Grew *et al.*, 2005), which has a composition very similar to kuratite except for the presence of Be (Table 3). Unit-cell data thus derived for kuratite show it is triclinic and in space group $P\bar{1}$ (by analogy to rhönite), $a = 10.513(7)$, $b = 10.887(7)$, $c = 9.004(18)$ Å, $\alpha = 105.97(13)$, $\beta = 96.00(12)$, $\gamma = 124.82(04)°$, $V = 767 \pm 2$ Å^3, $Z = 1$ for the formula with 40 oxygens. The $a{:}b{:}c$ ratio calculated from the unit-cell parameters is 0.966:1:0.827.

Powder X-ray diffraction data are not available for kuratite. Measured and refined *d*-spacings from TEM SAED patterns of section FIB-2 are listed in Table 2. The eight strongest reflections in electron diffraction, as ascertained from high-order zone-axis electron diffraction patterns of sections FIB-1 and FIB-2, are (in the order of decreasing *d* spacing, Å) 2.97 ($03\bar{1}$), 2.72 ($\bar{2}4\bar{1}$), 2.71 ($20\bar{3}$), 2.58 ($4\bar{2}0$), 2.57 ($21\bar{3}$), 2.45 ($22\bar{1}$), 2.13 ($\bar{2}5\bar{1}$) and 2.12 ($\bar{4}1\bar{1}$).

Raman spectroscopy

The Raman spectrum of kuratite, measured using a LABRAM HR confocal micro-Raman spectrometer equipped with an Ar+ laser with 514.5 nm excitation at Academia Sinica, Taiwan, shows four main scattering peaks near 563–571, 697–699 (strongest), 852–856 and 986–996 cm^{-1} (Fig. 4)

resembling that of lunar rhönite (Treiman, 2008) but with higher frequencies due to different chemical composition. A weak shoulder on the strongest peak at 720 cm^{-1} was recognized in lunar rhönite (Treiman, 2008) but was not present in kuratite.

Physical and optical properties

Calculated density is 3.906 g cm^{-3} using the empirical formula. Other physical properties and optical properties are not available because of the minute size of the kuratite crystals in the sample. The optical data available from the literature for Fe^{2+}-dominant rhönite, i.e. kuratite, are $\alpha = 1.805 \pm 0.007$, $\beta = 1.815 \pm 0.007$, $\gamma = 1.845 \pm 0.007$, $2V = 50 \pm 3°$ for Puy de St.-Sandoux rhönite ($X_{Mg} = 0.49$); $Z \wedge c = 38$–$43°$ for Kaiserstuhl rhönite ($X_{Mg} = 0.41$); $Z \wedge c = 58°$ ($X_{Mg} = 0.02$) for Luna 24 rhönite (Grapes and Keller, 2010; Grünhagen and Seck, 1972; Olsson, 1983; Treiman, 2008).

Discussion

Relation to other species

Rhönite is the only sapphirine-group mineral reported to have compositions with both Mg^{2+}/(Mg^{2+} + Fe^{2+}) < 0.5 and Mg^{2+}/(Mg^{2+} + Fe^{2+}) > 0.5. As plotted in figure 4 of Grapes and Keller (2010), there is a continuous range of Fe^{2+} and Mg substitution with Mg^{2+}/(Mg^{2+} + Fe^{2+}) = 0.16–0.49 for several terrestrial Fe^{2+}-rich rhönites; e.g. 'rhönite' in tephrite glass and limburgite of basaltic rocks from the Kaiserstuhl volcanic complex (Grapes and Keller, 2010), 'rhönite' in the unusual fassaite-melilite-rhönite paragenesis from an alkaline basalt contaminated by Ca from coral, Saint-Leu, Réunion Island (Havette *et al.*, 1982), 'rhönite' in the Mesozoic basanites from Skane (Scania) (Olsson, 1983), rhönite from a melaphonolite of Puy de Saint-Sandoux (Auvergne) (Grünhagen and Seck, 1972) and 'rhönite' in glass from kaersutite-bearing spinel-wehrlite xenoliths from Foster Crater (Gamble and Kyle, 1987). According to the 50% rule (Nickel and Grice, 1998), these so-called 'rhönite' phases could well be categorized as kuratite with the characteristic end-member composition Ca$_4$(Fe$^{2+}_{10}$Ti$_2$)O$_4$[Si$_8$Al$_4$O$_{36}$]. Note that kuratite was first anticipated in the paper reporting the nomenclature of the sapphirine supergroup (Grew *et al.*, 2008), in which the rhönites from Réunion, Skane, Puy de Saint-
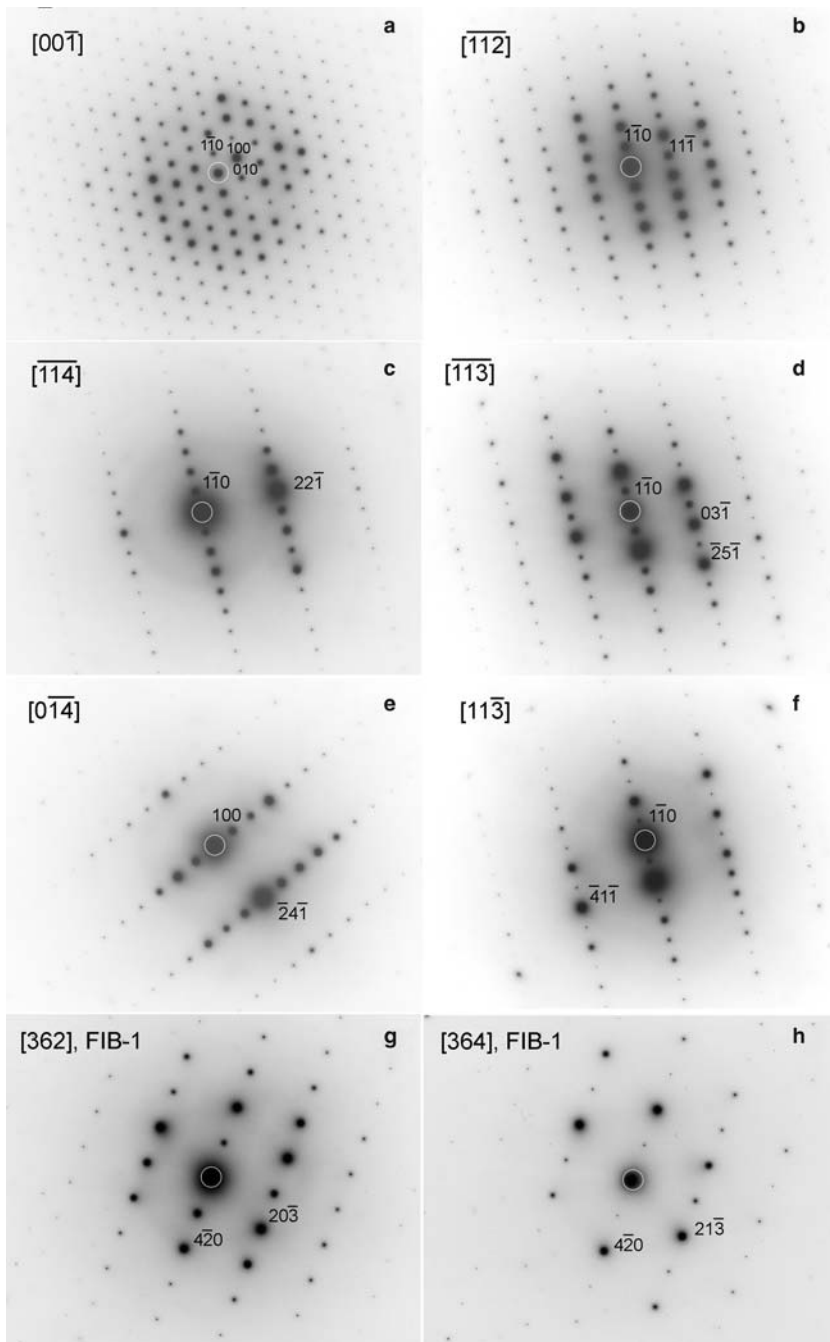
FIG. 3. Representative (*a,b*) low-order and (*c–f*) high-order zone-axis diffraction patterns of kuratite from section FIB-2 and (*g,h*) high-order zone-axis diffraction patterns from section FIB-1. The transmitted beam is circled in each diffraction pattern.

1073

TABLE 3. Comparison of unit-cell parameters between kuratite and other rhönite subgroup minerals.

	a (Å)	b (Å)	c (Å)	α (°)	β (°)	γ (°)	sample type
Kuratite $(Ca_{3.88}Na_{0.02}REE^{3+}_{0.03}Mn_{0.03}Mg_{0.01}Ni_{0.02}Zn_{0.01}Sr_{0.01})_{\Sigma4.01}(Fe^{2+}_{9.98}Ti_{2.00})_{\Sigma11.98}(Si_{7.80}Al_{3.52}Fe^{3+}_{0.64}P_{0.05}S_{0.02})_{\Sigma12.03}O_{39.98}F_{0.01}Cl_{0.01}$ $Ca(Fe^{2+}_{10}Ti_2)(Si_8Al_4)O_{40}$	10.5	10.9	9.0	106.0	96.0	124.8	D'Orbigny angrite
Rhönite $Ca_{3.8}Na_{0.2}(Mg_{6.6}Fe^{2+}_{1.2}Fe^{3+}_{2.2}Ti_2)(Si_6Al_6)O_{40}$ $Ca_4(Mg_8Fe^{3+}_2Ti_2)(Si_6Al_6)O_{40}$	10.4	10.8	8.9	105.9	96.1	124.8	volcanic breccias
Rhönite $Ca_4(Mg_{5.8}Fe^{2+}_{0.6}Ti^{3+}_{1.6}Al_{1.0}V_{0.6}Ti_{2.4})(Si_4Al_8)O_{40}$ $Ca_4(Mg_7Ti^{3+}_2Ti_3)(Si_4Al_8)O_{40}$	10.4	10.8	8.9	106.0	96.0	124.7	Allende meteorite
Makarochkinite[2] $(Ca_{3.28}Na_{0.50}Mn_{0.22})(Fe^{2+}_{7.12}Fe^{3+}_{2.92}Ti_{1.22}Mg_{0.50}Mn_{0.04}Nb_{0.076}Ta_{0.014})(Si_{8.96}Be_{1.82}Al_{1.08}Fe^{3+}_{0.14})O_{40}$ $Ca_4(Fe^{2+}_8Fe^{3+}_2Ti_2)(Si_8Be_2Al_2)O_{40}$	10.4	10.8	8.9	105.7	96.2	124.9	granitic pegmatite

[1]Bonaccorsi *et al.* (1990), [2]Grew *et al.* (2005).

Sandoux and Foster Crater were recognized as a distinct species, the Fe^{2+}-analogue of rhönite [see table 1 and figures 9 to 11 in Grew *et al.* (2008)].

As for the extraterrestrial occurrences, the first description of kuratite from a meteorite was made by Mittlefehldt *et al.* (2002) reporting the discovery of an unknown Fe-Al-Ti-silicate with a cation/Si ratio of ~2.65. Kurat *et al.* (2004) found the unknown Fe-Al-Ti silicate in multi-phase inclusions in anorthite, forming euhedral crystals up to 20 μm in diameter. This then unknown phase was also reported to be enclosed by augite and associated with magnetite, troilite and kirschsteinite. Its major chemical composition is homogeneous (Mittlefehldt *et al.*, 2002; Kurat *et al.*, 2004) and is characterized by high and unfractionated *REE* (~100 × CI) contents (Varela *et al.*, 2005). More recently, kuratite with $Mg^{2+}/(Mg^{2+} + Fe^{2+}) = 0$–0.17 was also found in the plutonic igneous angrite NWA 4590 (Kuehner and Irving, 2007), volcanic angrite SAHARA 99555 (Jambon and Boudouma, 2011), as well as magmatic inclusions in augite grains of the Luna 24 regolith (Treiman, 2008).

The ordering scheme in kuratite

For the rhönite subgroup minerals, it is well documented that in half of the unit cell, there are six different tetrahedral sites *T*1–*T*6, seven octahedral sites *M*1–*M*7, and two additional eightfold sites *M*8 and *M*9 (Bonaccorsi *et al.*, 1990; Grew *et al.*, 2008). The structure of rhönite minerals can be described as octahedral strips (*M*3–*M*7 octahedral sites and *M*8 and *M*9 eightfold sites) connected via tetrahedral chains with chain tetrahedra (*T*1–*T*4) and wings (*T*5 and *T*6 sites) and additional insular octahedra (*M*1 and *M*2). The octahedral strips are three to four octahedra wide
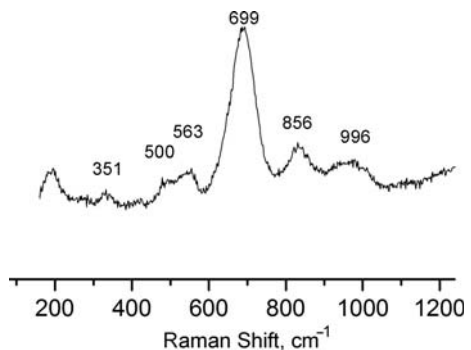

FIG. 4. Representative Raman spectrum of kuratite.

1074

and run parallel to the crystallographic a axis. The tetrahedral chains are pyroxene-like and aligned also along the a axis. The $M8$ and $M9$ sites are occupied by Ca. The Fe^{2+} and Mg^{2+} ions prefer $M1$ to $M6$ sites. Smaller Ti^{4+} ions are concentrated at the $M7$ site. As for the T sites, Si and Al probably occupy $T1$–$T4$ sites in equal proportion, and $T5$ and $T6$ are dominantly Si (Grew et $al.$, 2008, and references therein). Although it is not possible to determine the structure of kuratite directly due to its minute crystal size, the close similarity in crystal chemistry, unit-cell type and parameters between kuratite and rhönite subgroup minerals, e.g. rhönite and makarochkinite (Table 3), do indicate that kuratite should be similar to rhönite and makarochkinite in every aspect; Ca at $M8$ and $M9$, Fe^{2+} at $M1$–$M6$, Ti at $M7$, Si and Al at $T1$–$T6$. By comparison with the site occupancies in makarochkinite $(Ca_4(Fe_8^{2+}Fe_2^{3+}Ti_2)(Si_8Be_2Al_2)O_{40})$ with similar Fe/Ti ratio at M sites and the Si/(Be + Al) ratio at T related to kuratite, Ti^{4+} is probably ordered at the $M7$ site in kuratite, whereas Fe^{2+} are disordered over the $M1$–$M6$ sites (Grew et $al.$, 2005).

Origin of kuratite in the angrite meteorite

The formation of the angrite meteorite is still under debate, although most studies favour a basaltic igneous origin (Keil, 2012). Following the igneous scenario, it is not surprising that kuratite was found in angrite D'Orbigny, plutonic igneous angrite NWA 4590 (Kuehner and Irving, 2007), volcanic angrite SAHARA 99555 (Jambon and Boudouma 2011) and Luna 24 regolith (Treiman 2008), similar to the common occurrences of other Fe^{2+}-dominant rhönites in terrestrial undersaturated basaltic rocks such as tephrite and limburgite from volcanic complexes (Grapes and Keller, 2010), basanite glass in spinel-wehrlite xenoliths (Gamble and Kyle, 1987), alkaline basalt within coral (Havette et $al.$, 1982) and basanite (Olsson, 1983). In fact, texture observations indicate that terrestrial kuratite in basaltic rocks was the last phase crystallized. The frequent presence of glass groundmass further indicates that kuratite was most likely a quench phase either on eruption (e.g. undersaturated alkaline basaltic rocks; Grapes and Keller, 2010) or from rapid cooling of an infiltrated melt into the host rocks (e.g. kaersutite-bearing wehrlite xenoliths; Gamble and Kyle, 1987). In accordance with the above, the occurrence of kuratite + whitlockite embedded in Ca-rich fayalite + kirschsteinite

intergrowths (Fig. 1d,e) at the contact between Fe-sulfide spherules and hedenbergite suggests that these phases could have crystallized from an interstitial melt at a very late stage of rock formation. Although it is not clear regarding the origin of this interstitial melt phase, i.e. residue from fractional crystallization or a fresh, infiltrating melt (Mittlefehldt et $al.$, 2002; Kurat et $al.$, 2004; Varela et $al.$, 2003), this interstitial melt must be subsilicic, almost Mg-free but enriched in Al-P-Ca-Ti-Fe. Alternatively, the multiple phase assemblage at olivine-augite triple junctions might represent metasomatic products resulting from reactions between an intruding metasomatic agent, which could be either gas, liquid or melt, and the porous and fractured olivine + augite + Fe-sulfide aggregates (see Fig. 1a). In either case, the crystallization temperatures of kuratite must be >1000°C, considering the co-presence of Ca-rich fayalite and kirschsteinite (Mukhopadhyay and Lindsley, 1983), the 950–1180°C stability field of rhönites based on experimental phase relations for various undersaturated alkaline basaltic rocks (Kunzmann, 1999), and the environment for the formation of Fe^{2+}-dominant rhönite as a quenched phase in glass with liquidus temperatures of 1038–1137°C in tephrite and limburgite bulk compositions (Grapes and Keller, 2010).

Acknowledgements

References

Bonaccorsi, E., Merlino, S. and Pasero, M. (1990) Rhönite: structural and microstructural features, crystal chemistry and polysomatic relationships. $European$ $Journal$ of $Mineralogy$, **2**, 203–218.

Gamble, J.A. and Kyle, P.R. (1987) The origins of glass and amphibole in spinel-wehrlite xenoliths from Foster Crater, McMurdo Volcanic Group, Antarctica. $Journal$ of $Petrology$, **28**, 755–779.

Grapes, R. and Keller, J. (2010) Fe^{2+}-dominant rhönite in undersaturated alkaline basaltic rocks, Kaiserstuhl volcanic complex, Upper Rhine Graben, SW Germany. $European$ $Journal$ of $Mineralogy$, **22**, 285–292.

Grew, E.S., Barbier, J., Britten, J., Yates, M.G., Polyakov, V. O., Shcherbakova, E.P., Hålenius, U. and Shearer, C.K. (2005) Makarochkinite, $Ca_2Fe_4^{2+}Fe^{3+}TiSi_4BeAlO_{20}$, a new beryllosilicate member of the aenigmatite-

sapphirine-surinamite group from the Il'men Mountains (southern Urals), Russia. *American Mineralogist*, **90**, 1402–1412.

Grew, E.S., Hålenius, U., Pasero, M. and Barbier, J. (2008) Recommended nomenclature for the sapphirine and surinamite groups (sapphirine supergroup). *Mineralogical Magazine*, **72**, 839–876.

Grünhagen, H. and Seck, H.A. (1972) Rhönite aus einem Melaphonolith vom Puy de Saint-Sandoux (Auvergne). *Tschermaks Mineralogische und Petrographische Mitteilungen*, **18**, 17–38.

Havette, A., Clocchiatti, R., Nativel, P. and Montaggioni, L.F. (1982) Une paragenèse inhabituelle à fassaïte, mélilite et rhönite dans un basalte alcalin contaminé au contact d'un récif coralline (Saint-Leu, Ile de la Réunion). *Bulletin de Minéralogie*, **105**, 364–375.

Hwang, S.-L., Shen, P., Chu, H.-T., Yui, T.-F., Varela, M.E. and Iizuka, Y. (2015) Tsangpoite, IMA 2014-110. CNMNC Newsletter No. 25, June 2015, page 533; *Mineralogical Magazine*, **79**, 529–535.

Jambon, A. and Boudouma, O. (2011) Evidence for rhönite in angrites D'Orbigny and Sahara 99555 (abstract). *Meteoritics and Planetary Science*, **46 Supplement**, A113.

Keil, K. (2012) Angrites, a small but diverse suite of ancient, silica-undersaturated volcanic-plutonic mafic meteorites, and the history of their parent asteroid. *Chemie der Erde*, **72**, 191–218.

Kuehner, S.M. and Irving, A.J. (2007) Primary ferric iron-bearing rhönite in plutonic igneous 232 angrite NWA 4590: implications for redox conditions on the angrite parent body. *Eos, AGU*, 88, *Fall Meeting Supplement*, Abstract P41A-0219.

Kunzmann, T. (1999) The aenigmatite-rhönite mineral group. *European Journal of Mineralogy*, **11**, 743–756.

Kurat, G., Varela, M.E., Brandstätter, F., Weckwerth, G., Clayton, R., Weber, H.W., Schultz, L., Wäsch, E. and

Nazarov, M.A. (2004) D'Orbigny: A non-igneous angritic achondrite? *Geochimica et Cosmochimica Acta*, **68**, 1901–1921.

Mittlefehldt, D.W., Killgore, M. and Lee, M.T. (2002) Petrology and geochemistry of D'Orbigny, geochemistry of Sahara 99555, and the origins of angrites. *Meteoritics and Planetary Science*, **37**, 345–369.

Mukhopadhyay, D.K. and Lindsley, D.H. (1983) Phase relations in the join kirschsteinite ($CaFeSiO_4$)–fayalite (Fe_2SiO_4). *American Mineralogist*, **68**, 1089–1094.

Nickel, E.H. and Grice, J.D. (1998) The IMA Commission on New Minerals and Mineral Names: procedures and guidelines on mineral nomenclature. *The Canadian Mineralogist*, **36**, 913–926.

Olsson, H.B. (1983) Rhönite from Skåne (Scania), southern Sweden. *Geologiska Föreningen i Stockholm Förhandlingar*, **105**, 281–286.

Smith, D.G.W. and Nickel, E.H. (2007) A system for codification for unnamed minerals: report of the Subcommittee for Unnamed Minerals of the IMA Commission on New Minerals, Nomenclature and Classification. *The Canadian Mineralogist*, **45**, 983–1055.

Treiman, A.H. (2008) Rhönite in Luna 24 pyroxenes: first find from the Moon, and implications for volatiles in planetary magmas. *American Mineralogist*, **93**, 488–491.

Varela, M.E., Kurat, G., Zinner, E., Métrich, N., Brandstätter, F., Natflos, T. and Sylvester, P. (2003) Glasses in the D'Orbigny angrite. *Geochimica et Cosmochimica Acta*, **67**, 5027–5046.

Varela, M.E., Kurat, G., Zinner, E., Hoppe, P., Ntaflos, T. and Nazarov, M.A. (2005) The non-igneous genesis of angrites: support from trace element distribution between phases in D'Orbigny. *Meteoritics and Planetary Science*, **40**, 409–430.